



Final Draft **of the original manuscript**

Xu, X.; Ran, Q.; Haag, R.; Ballauff, M.; Dzubiella, J.:

Charged Dendrimers Revisited: Effective Charge and Surface Potential of Dendritic Polyglycerol Sulfate.

In: *Macromolecules*. Vol. 50 (2017) 12, 4759 - 4769.

First published online by ACS: 13.06.2017

<http://dx.doi.org/10.1021/acs.macromol.7b00742>

Charged dendrimers revisited: Effective charge and surface potential of dendritic polyglycerol sulfate

Xiao Xu,^{†,‡,¶} Qidi Ran,^{†,¶,§} Rainer Haag,^{¶,§} Matthias Ballauff,^{†,‡,¶} and Joachim Dzubiella^{*,†,‡,¶}

[†]Institut für Weiche Materie und Funktionale Materialien, Helmholtz-Zentrum Berlin, Hahn-Meitner-Platz 1, 14109 Berlin, Germany

[‡]Institut für Physik, Humboldt-Universität zu Berlin, Newtonstr. 15, 12489 Berlin, Germany

[¶]Multifunctional Biomaterials for Medicine, Helmholtz Virtual Institute, Kantstr. 55, 14513 Teltow-Seehof, Germany

[§]Institut für Chemie und Biochemie, Freie Universität Berlin, Takustr. 3, 14195 Berlin, Germany

E-mail: joachim.dzubiella@helmholtz-berlin.de

Abstract

We investigate key electrostatic features of charged dendrimers at hand of the biomedically important dendritic polyglycerol sulfate (dPGS) macromolecule using multi-scale computer simulations and Zetasizer experiments. In our simulation study, we first develop an effective mesoscale Hamiltonian specific to dPGS based on input from all-atom, explicit-water simulations of dPGS of low generation. Employing this in coarse-grained, implicit-solvent/explicit-salt Langevin dynamics simulations, we then study dPGS structural and electrostatic properties up to the sixth generation. By systematically mapping then the calculated electrostatic potential onto the Debye-Hückel form – that serves as a basic defining equation for the effective charge – we determine well-defined effective net charges and corresponding radii, surface charge densities, and surface potentials of dPGS. The latter are found to be up to one order of magnitude

smaller than the bare values and consistent with previously derived theories on charge renormalization and weak saturation for high dendrimer generations (charges). Finally, we find that the surface potential of the dendrimers estimated from the simulations compare very well with our new electrophoretic experiments.

1. INTRODUCTION

Charged dendritic macromolecules have attracted strong and broad interest from both academic and industrial researchers due to their versatile bioapplications, such as drug delivery, tissue engineering, and biological imaging.¹⁻³ Recently, a high potential candidate for the use in future medical treatments has been identified based on dendritic polyglycerol sulfate (dPGS).⁴ The latter has been found very efficient for the treatment of neurological disorders arising from inflammation,⁵ therapeutics for preventing the process of tissue damage,⁶ acting as delivery platform,^{7,8} e.g., transporting to tumor cells,⁹ and as imaging agent for the diagnosis of rheumatoid arthritis.⁸ Due to its charged terminal groups dPGS interacts mainly through electrostatics. The high anionic surface charge is therefore basis for dPGS' high anti-inflammatory potential.^{10,11}

The important applications of dendrimeric macromolecules have initiated large efforts in their detailed microscopic characterization by theory and computer simulations.^{1,3} While there is no simulation work yet in literature characterizing the basic structural features of dPGS, a large number of atomistic computer simulations, for example, of PAMAM [poly(amidoamine)]-based dendrimers have been performed.¹²⁻¹⁷ On the other hand, to overcome the limitation of the system size of atomistic simulations, coarse-grained (CG) monomer-resolved models with more or less inclusion of specific chemical features have led to plentiful structural insight.¹⁸⁻⁴³ For the case of (internally and surface) charged dendrimers, one focus has been set on the dominant role of condensed counterions and charge renormalization⁴⁴⁻⁵¹ in modulating the conformation and effective charge of the dendrimers.³⁹⁻⁴³

However, it has been hardly attempted to consistently calculate the effective surface potential (and

its location) of charged dendrimers so far, despite its significance for electrostatic interactions. One reason could be that the identification of condensed counterions requires the definition of a cut-off region in space that contains condensed-types of ions distinct from those in the diffusive double layer, with highly varying definitions in the just cited literature. As a consequence, effective charges and the spatial delimitation of diffusive double-layer behavior have been inconsistently defined, hampering a meaningful comparison to analytical theory and experiments. Regarding specifically the calculation of surface potentials, one notable exception is the simulation report on charged PAMAM dendrimers that revealed a superlinear increase of the effective charge and the surface potential with generation number.¹⁷ In view of the theoretically predicted saturation (or at least very weak, sublinear increase) of the effective charge with bare charge for simple charged spheres,⁴⁴⁻⁵¹ this result, however, is unexpected and not well understood. In fact, in the case of carboxyl-terminated dendrimers capillary electrophoretic experiments demonstrated that higher generation dendrimers (generation 5) even have a smaller effective surface charge than lower generations (generation 2).⁵² Hence, despite the large body of studies on charged dendrimers in the last two decades, key electrostatic features have not been yet consistently addressed.

Driven by the urgent need to develop accurate modeling tools and interpretation for the interactions between charged dendritic drugs that are predominantly of electrostatic nature, we here investigate dPGS with a particular focus on the determination of its electrostatic surface properties. Compared to the relatively large and steady growing number of experimental publications on dPGS, a deeper molecular characterization of dPGS is still lacking. Hence, in this paper, based on all-atom MD simulations, a CG model specific to dPGS is reported for its future modeling in biological environments (e.g., interacting with proteins or membranes). In particular, we introduce a simple but accurate scheme how to systematically calculate well-defined effective surface charges and potentials of charged dendrimers in the case of dPGS based on the most practical definition by mapping the calculated potentials directly to the Debye-Hückel potential in the far-field regime. We compare them to available theories and new experimental ζ -potential measurements (also included in this contribution) with consistent outcome. Our study thus paves the way for future simulations

and interpretations of the dPGS' and related dendritic polyelectrolytes' action in biological context (e.g., interacting with proteins or membranes) to understand and optimize their proven selective binding properties and efficacy in the medical treatment of inflammatory diseases.

2. MODELS AND METHODS

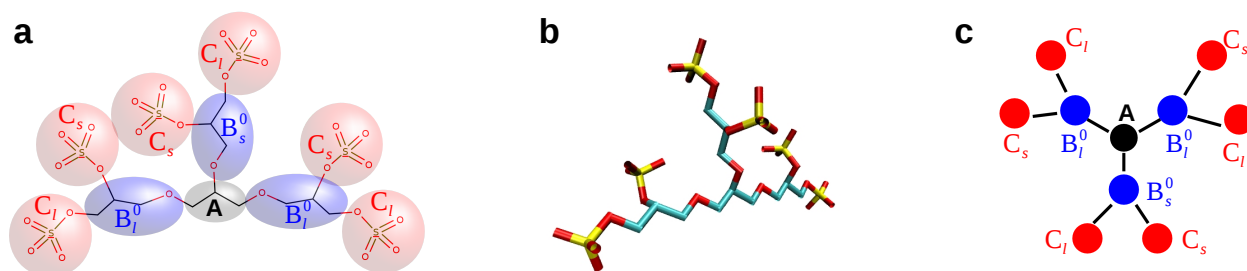


Figure 1: (a) Chemical formula, (b) atomistic structure, and (c) coarse-grained (CG) structure sketch of the zeroth generation G_0 -dPGS molecule. In panel (a), we depict the atomistic subunits C_3H_5 , C_3H_7O , and SO_4^- corresponding to the CG bead types A, B_i , and C_i ($i = s, l$) in panel (c) by the black, blue, red colored regions, respectively.

2.1. All-atom model and explicit-water MD simulations. We start the development of the dPGS coarse-grained (CG) force-field from fully atomistic (explicit-water) MD simulations of dPGS of generations $n = 0$ and 1 (i.e., G_0 and G_1) from which effective intra-bead potentials are derived. The constituting elements are the initiator core C_3H_5 , repeating side chain units C_3H_5O , as well as the terminal sulfate groups, see the exemplary chemical structure of G_0 , in Fig. 1. All our simulations are carried out by the GROMACS 4.5.4 software package,⁵³ where the GROMOS 45a3 force field⁵⁴ is applied. The latter is optimized to model lipids with long aliphatic chains or branches, which makes it an appropriate force field to model dPGS. The water is represented by the extended simple point charge (SPC/E) model.⁵⁵ The partial charges of dPGS are calculated according to the Gaussian 09 software⁵⁶ with the cc-PVTZ DFT basis set and used here in combination with the GROMOS 45a3 force field. The assigned partial charges among the glycerol groups stay close to the re-optimized parameters for ethers.⁵⁷ And those for the sulfate group agree with recent work⁵⁸ which have been applied, for instance, in the simulation of sodium dodecyl sulfate micelles.⁵⁹ The

calculations of partial charges of the dPGS atoms and the influence of their particular choices on the dendrimeric structure are summarized in the Supplementary Information (SI).

The initial configurations of G_0 and G_1 -dPGS are constructed in vacuum with the program Chem-Draw.⁶⁰ A single dendrimer is then placed in the center of a cubic simulation cell with an initial side length $L = 7.9$ nm with periodic boundary conditions in all three directions. The dendrimer is subsequently hydrated with 16543 water molecules. To preserve the overall charge neutrality of G_0 and G_1 , six or twelve Na^+ -counterions are added, respectively. The electrostatic interactions are calculated via the Particle-Mesh-Ewald (PME)⁶¹ summation where the long-range potential is evaluated in the reciprocal space using the Fast-Fourier Transform (FFT) with a grid spacing of 0.16 nm and a cubic interpolation of fourth order. A cut-off radius of 1 nm is defined for both PME summation and van der Waals real-space interactions. After a 100 ns equilibration in the isobaric NPT ensemble at conditions of $P = 1$ bar and $T = 310$ K, a production run of 1 μs generates a working trajectory in a canonical NVT simulation. We utilize the Berendsen thermostat and the Rahman-Parrinello barostat. To integrate Newton's equation of motion we employ the leap-frog algorithm with a time step of 2 fs.

2.2. Coarse-graining procedure . For our CG model we now define three coarse-grained bead types A, B, and C, chosen to be located at the center-of-mass position of repeating units, cf. Fig. 1. While type A simply models the central core unit (C_3H_5), the natural choice for B and C is reflected in the chemical formula $\text{C}_3\text{H}_5(\text{C}_3\text{H}_5\text{S}_2\text{O}_9)_3$ for G_0 -dPGS which defines the repeating units $\text{C}_3\text{H}_5\text{O}$ as type B and the terminal group SO_4 as monomer C. As one can see in the chemical structure in Fig. 1, the intra-bead potentials between B and C beads (as well as between B and B beads in higher generations) depend on how the corresponding atomistic groups are connected: in a given triplet of units around a connecting central hub unit, two units feature an extra bond so that it is needed to introduce 'short' and 'long' bead types B and C for intermediate branching cycles $m = 0..n$. In the following we therefore distinguish between B_s^m and B_l^m as well as C_s and C_l beads, respectively. Hence, for the coarse-grained force field we need to define bond potentials of

types $A-B_j^0$, $B_i^m-B_j^{m+1}$, $B_i^n-C_j$, with $i = s, l$ and angle potentials for all relevant triplets, for example, $A-B_i^0-B_j^1$, $B_i^m-B_j^{m+1}-B_k^{m+2}$, $B_i^{m+1}-B_j^m-B_k^{m+1}$, $B_i^{n-1}-B_j^n-C_k$, etc. Note that there must be 'up-down' symmetry in the potentials, e.g., $B_i^m-B_j^{m+1}=B_i^m-B_j^{m-1}$ for the bond potentials and analogous rules for the angular potentials. Finally, non-bonded inter-bead interactions have to be defined between types A, B, and C.

We employ harmonic potentials for the intramolecular (bond and angular) interactions and use the Lennard-Jones (LJ) interaction for all inter-bead potentials. Additionally, the beads of type C and ions carry charges. Hence, the CG force field can be formally summarized by the CG Hamiltonian

$$\begin{aligned}
U^{\text{CG}} = & \sum_{\text{bonds}} \frac{1}{2} k_b (l - l_0)^2 + \sum_{\text{angle}} \frac{1}{2} k_a (\theta - \theta_0)^2 \\
& + \sum_{i < j} 4\epsilon_{ij} \left[\left(\frac{\sigma_{ij}}{r_{ij}} \right)^{12} - \left(\frac{\sigma_{ij}}{r_{ij}} \right)^6 \right] + U_{\text{elec}}.
\end{aligned} \tag{1}$$

where r_{ij} is the bead-bead distance, k_b and k_a are the bond and angular spring constants, respectively, l represents the distance between consecutive beads and l_0 is the equilibrium bond length. The variable θ refers to the angle formed by a triplet of consecutive beads and θ_0 is the equilibrium value. Only the C bead, representing the terminal sulfate group, carries a bare Coulomb charge $q_s = -e$. It follows that the net charge valency for the CG dPGS molecule of generation n is $Z_{\text{bar}} = -6(2^{n+1} - 2^n)$ and thus the terminal beads number $N_{\text{ter}} = |Z_{\text{bar}}|$. The electrostatic interactions for all charged beads (type C and ions) are included in U_{elec} , via the Coulomb law

$$U_{\text{elec}} = \sum_{i=1}^{N_{\text{ter}}+N_{\text{ion}}} \sum_{j=1, j \neq i}^{N_{\text{ter}}+N_{\text{ion}}} \frac{l_B}{2r_{ij}}. \tag{2}$$

The variable $l_B = e^2 / (4\pi\epsilon_0\epsilon_r k_B T)$ stands for the Bjerrum length, which is $l_B = 0.7$ nm in this study at body temperature $T = 310$ K and for water with a permittivity constant $\epsilon_r = 78.2$, N_{ion} denotes the number of ions, e is the elementary charge, and ϵ_0 is the permittivity of vacuum.

We derive the bonded potentials by Boltzmann-inverting the corresponding target spatial distribu-

tion functions of the beads $f(x)$ we obtain from the atomistic MD simulation, via

$$U(x) = -k_B T \ln f(x), \quad (3)$$

where x is either a bond length or angle variable and $f(x)$ is an equilibrium average over the fluctuations of all identical groups in the dendrimer. All potentials involving beads A and C are derived from simulations of G_0 . All potentials involving beads only of type B are derived from simulations of G_1 as B-B bonds are absent in G_0 . The results and final parameters of the bonded CG potentials are discussed and summarized in the next section.

The extraction of the non-bonded A-A, B-B and C-C potentials directly from the atomistic MD simulation of G_0 or G_1 -dPGS is very difficult due to the convoluted spatial structure of the dendritic dPGS. Therefore, a mapping using the iterative Boltzmann inversion (IBI) scheme^{62,63} is out of reach. We therefore resort to the simplest approximation and perform explicit-water simulations of a one-component fluid of isolated A, B, and C monomers in explicit water, respectively, at relatively high dilution. The respective non-bonded pair potentials are then obtained by the simple Boltzmann-inversion according to Eq. (3), where $f(x)$ then simply represents the radial distribution function. The charged sulfate monomers corresponding to subunit C are protonated to separate out approximately the electrostatic monopole repulsion which later in the CG simulation are added again. The partial charges of the A, B, C chemical subunits are calculated according to the Gaussian 09 software⁵⁶ with the cc-PVTZ DFT basis set, and used here in combination with the GROMOS 45a3 force field, see the data in the SI. We set the concentration of the one-component bead fluid to $c \sim 400$ mM that is chosen high enough to obtain sufficient sampling and low enough to avoid large many-body effects and possibly aggregated states. After obtaining the LJ parameters ϵ_{ii} and σ_{ii} by fitting the LJ potentials to the obtained effective interaction (see next section) for the three subunits, $i = A, B, C$, the corresponding values for the cross interactions are obtained by the conventional Lorentz-Berthelot mixing rules, i.e., $\sigma_{ij} = (\sigma_{ii} + \sigma_{jj})/2$ and $\epsilon_{ij} = \sqrt{\epsilon_{ii}\epsilon_{jj}}$.

The simple Boltzmann-inversion scheme for the inter-bead potentials that neglects many-body

and connectivity effects is approximative. However, the excluded-volume part of the LJ is hardly affected by this treatment, only the attractive (van der Waals) part of the LJ interaction is expected to be affected by the many-body contributions. (Note that most CG simulations in the literature do not include the van der Waals attraction.) Therefore, we tested the influence of varying the bead ϵ_{ii} on some of the key structural and electrostatic of the dendrimers. The results (presented in the SI) show hardly any influence on the results for dispersion variations in a reasonable window and therefore leave our results quantitatively essentially unchanged.

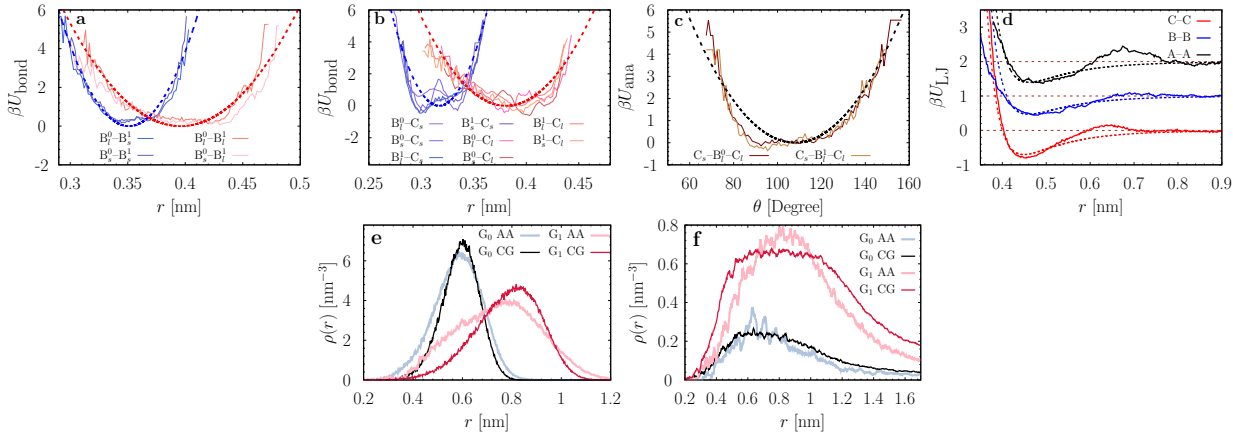


Figure 2: The (a) $B_i^0-B_j^1$ bond, (b) $B_i^m-C_j$ bond, (c) $C_i-B_j^m-C_k$ angular ($m = 0$ for G_0 and $m = 1$ for G_1), and (d) A-A/B-B/C-C effective inter-bead potentials extracted from the all-atom MD simulations (AA; solid lines). The dashed lines are the fits according to the coarse-grained (CG) Hamiltonian Eq. (1). For the atomistic simulations, the coordinate r is defined as the bead-bead center-of-mass distance. The indices $i, j = s, l$ distinguish between beads having short or long bond connections in the molecular structure, respectively. In the bottom panels the density distributions of the terminal sulfate groups (e) and counterions (f) around the dPGS center-of-mass from atomistic and CG simulations are compared for the G_0 and G_1 dPGS, respectively. The simulations were performed at salt concentrations $c = 30$ mM for G_0 and $c = 50$ mM for G_1 .

2.3. Coarse-grained potentials. Selected results of our mapping procedure are plotted in Fig. 2.

As we see in panels (a) to (c), the intra-bond potentials can be fitted well by a harmonic function. We find that the asymmetry in the glycerol repeat unit leads to an equilibrium bond length that differs if ‘short’ or ‘long’ beads are connected at the upper cycle branch $m + 1$. The shift between the bond lengths corresponds to a single covalent bond length on the Ångstrom scale. The structure asymmetry is also reflected in the angular potential U_{ana} (provided in the SI), although in that case

the effect is less notable as compared to the bond potential. As shown in Fig. 2(c), the angle θ formed by a triplet of monomers C–B–C has a distribution ranging from 60° to 150° and is thus relatively broad when compared to typical atomistic potentials. Note that in all of the previous CG dendrimers models angular potentials were typically neglected. All bonded bead potentials are summarized in Table 1.

In Fig. 2(d), we present the non-bonded LJ potentials between pairwise groups A-A, B-B, and C-C. At small separation, $r \lesssim 0.4$ nm, a strong repulsion demonstrates the excluded-volume interaction, while in the intermediate distance $r \simeq 0.6$ to 0.7 nm, a small energy barrier signifies effects of the first hydration shell around the beads. We neglect these small barriers and fit the curve via the LJ potentials, cf. the dashed lines in Fig. 2 (d). The final parameters for the CG ϵ_{ij} and σ_{ij} values for all three bead types are very similar. This can be seen as a justification to set a generic LJ potential for all CG beads as typically utilized in previous CG studies of monomer-resolved dendrimers.^{1,30,31,33}

We complement the CG force-field by effective potentials for a symmetric monovalent salt where, for simplicity, we chose the same LJ parameters as for the charged C bead. The corresponding LJ size for the ions is actually the same as for the effective CG sodium-chloride cross interaction in water,^{64,65} so it seems a reasonable choice to model a simple monovalent salt. The relatively small energy parameter ϵ_{LJ} parameter of 0.1 kJ/mol models hard-sphere like ions without any strong ion pairing behavior.⁶⁵ The parameters for the non-bonded interaction are summarized in Table 2.

In order to further scrutinize the validity of the CG force field, we compare density profiles of the terminal sulfate groups, Fig. 2(e), and the cations, Fig. 2(f), extracted from atomistic and CG simulations (see next section for methods) of generation $n = 0$ and 1. A good agreement is reached between the two approaches in both profiles for both generations, consolidating earlier conclusion on the validity of CG force field for charged dendrimers.⁴² For G_1 , we find that the width of the distribution of the terminal groups appears to be a bit narrower in the CG force field. Yet, the global structure represented by the location of the density peaks appears to be similar for both approaches. This similarity applies to the counterion distribution as well, indicated by the density peak at $r \sim 0.82$ nm produced by both levels of modeling.

Table 1: Parameter for the CG dPGS bonded potentials. The subscript s and l refers to B_i beads with a long or short glycerol arm, respectively. $m = 0$ to n denominates the intermediate branching cycle for a given generation n .

| group | k_b ($k_B T \text{ nm}^{-2}$)(nm) | l_0 (nm) | k_a ($k_B T \text{ deg}^{-2}$)(deg) | θ (deg) |
|---------------------------|--|---------------|--|-------------------|
| $A-B^0$ | 1381 | 0.380 | – | – |
| $A-B_s^0$ | 5100 | 0.337 | – | – |
| $B_{s,l}^m-B_l^{m+1}$ | 1052 | 0.395 | – | – |
| $B_{s,l}^m-B_s^{m+1}$ | 3105 | 0.351 | – | – |
| $B_{s,l}^n-C_l$ | 1633 | 0.380 | – | – |
| $B_{s,l}^n-C_s$ | 6160 | 0.312 | – | – |
| $B_{s,l}^0-A-B_{s,l}^0$ | – | – | 0.003 | 115 |
| $B_{s,l}^1-B_{s,l}^0-A$ | – | – | 0.003 | 115 |
| $B_{s,l}-B_{s,l}-B_{s,l}$ | – | – | 0.003 | 115 |
| $C_{s,l}-B_{s,l}^n-$ | – | – | 0.003 | 121 |
| $B_{s,l}^{n-1}$ | – | – | – | – |
| $C_{s,l}-B_{s,l}^0-A$ | – | – | 0.003 | 121 |
| $C_s-B_{s,l}^n-C_l$ | – | – | 0.005 | 108 |

Table 2: CG dPGS nonbonded potential.

| group | σ_{LJ} (nm) | ϵ_{LJ} ($k_B T$) |
|--------|--------------------|-----------------------------|
| A | 0.41 | 0.60 |
| B | 0.41 | 0.53 |
| C | 0.40 | 0.70 |
| cation | 0.40 | 0.10 |
| anion | 0.40 | 0.10 |

2.4. Coarse-grained simulations. Having established a CG force field, all generations n of dPGS can be now readily constructed. Higher generations G_n with index $n > 0$ are created by iteratively bonding two extra glycerol units to the original one (dendritic segment) on the outer shell of generation G_{n-1} . This Cayley tree-like⁶⁶ structure gives an exponentially growing of the polymerization $N_g = 3(2^{n+1} - 1) + 1$ with its generation index n , which thereby leads to the sulfate group number $N_{\text{ter}} = 6(2^{n+1} - 2^n)$ and the gross number $N_{\text{dP}} = 6 \times 2^{n+1} - 2$ of the CG segments. Note the above structure only fits to a perfect dendrimer, whereas an imperfect dendrimer bears a small number of linear segments that corresponds to most experimental dPGS realizations.¹⁰ In our work we investigate seven different generations $n = 0$ up to $n = 6$, depicted and with some features summarized in Table 4.

For the CG simulations the dPGS macromolecules are placed in a cubic box with a side length of $L = 35$ nm with periodic boundary conditions in all three directions. We treat the solvent implicitly via a uniform dielectric background, however, ions are treated explicitly to account for ionic correlation effects. In view of the charge status of dPGS, a number of monovalent counterions, $n_c = 6(2^{n+1} - 2^n)$, is added to maintain an electroneutral system. Apart from the counterions, in all simulations, dPGS is immersed in a salt solution with $N_i = 257$ to 5140 pairs of monovalent cations and anions, resulting into bulk salt concentrations from $c_0 = N_i/L^3 \simeq 10$ mM to 200 mM. The initial dendrimer configuration is assembled according to the equilibrium bond length l_0 and angle θ_0 appeared in Eq. (1).

We perform Langevin dynamics simulations on CG dPGS of generation number ranging from 0 to 6 also using the GROMACS package. All the implicit water simulations used the second-order stochastic dynamics (SD) integrator in GROMACS with the friction in the Langevin equation set with a time constant of $\tau_f = 1$ ps and integration time of 2 fs. We set all CG beads to have a small mass of $m_i = 0.5$ amu to decrease inertial effects and lower the intrinsic viscosity (i.e., internal relaxation time) of the dPGS. Equilibrium properties, as investigated in this work, are not affected by any reasonable mass choices as long as the simulations are ergodic. With an increasing number of the terminal beads the electrostatic interaction becomes more profound and the cut-off radius

for the PME summation and short-range van der Waals interactions is extended to $r_{\text{cut}} = 4$ nm as compared to the above atomistic simulation. The choice of the cutoff is verified by reference simulations with increased cutoff value $r_{\text{cut}} = 6.0$ nm. Unless specifically stated otherwise, the temperature was set to 310 K as the default. The static dielectric constant of the solvent is $\epsilon_r = 78.2$ at this temperature. After energy minimization of the initial structure and a 1 ns equilibration period, the production run of a *NVT* simulation lasts around 60 ns. That time has been proven to be sufficient for equilibrium sampling for all generations as in detail verified in the SI by scrutinizing relaxation times and time unit scalings between all-atom and CG simulations.

2.5. Analysis of the CG simulations.

2.5.1 dPGS radius of gyration and asphericity

The size of a dendrimer can be characterized by the radius of gyration R_g which is defined as the trace of the gyration tensor (\mathbf{R}^2)²⁹

$$\mathbf{R}_{\alpha,\beta}^2 = \frac{1}{N_{\text{dP}}} \sum_{i=1}^{N_{\text{dP}}} (\mathbf{r}_\alpha^i - \mathbf{r}_\alpha^M)(\mathbf{r}_\beta^i - \mathbf{r}_\beta^M), \quad \alpha, \beta = x, y, z, \quad (4)$$

where \mathbf{r}_α^i is the coordinate of the i th segment and \mathbf{r}_α^M is the dPGS COM position along the α direction. The square of the radius of gyration is then

$$R_g^2 = \langle \text{tr}(\mathbf{R}^2) \rangle = \left\langle \sum_{i=1}^3 \lambda_i^2 \right\rangle, \quad (5)$$

where λ_i^2 is the i th eigenvalue of the gyration tensor, representing the characteristic length of the equivalent ellipsoid which mimics the dendrimer. $\langle \dots \rangle$ stands for the ensemble average. The degree of asphericity A of dPGS is defined in terms of the eigenvalue λ_i^2 , which can be written as

$$A = \frac{\langle (T_r^2 - 3M) \rangle}{\langle T_r^2 \rangle}, \quad (6)$$

with $T_r = \lambda_1^2 + \lambda_2^2 + \lambda_3^2$ and $M = \lambda_1^2\lambda_2^2 + \lambda_2^2\lambda_3^2 + \lambda_1^2\lambda_3^2$. For a perfect sphere A equals 0, whereas $A = 1$ corresponds to the extreme of an infinitely thin rod.

2.5.2 The radial electrostatic potential

The electrostatic potential ϕ is available through the framework of Poisson's equation

$$\nabla^2 \phi = - \sum_{i=+, -, C} Z_i \rho_i(r) / \epsilon_0 \epsilon_r, \quad (7)$$

where in our CG system $\rho_+(r)$, $\rho_-(r)$ and $\rho_C(r)$ are the distance-resolved radial density profiles for all charged species, namely cations, anions and sulfate (C) beads, respectively. We integrate Poisson's equation numerically feeding in the $\rho_i(r)$ generated from simulation to obtain the local electrostatic potential $\phi(r)$. In addition to the potential profile, we calculate the running coordination number of charged beads of type $i = \pm, C$:

$$N_i(r) = \int_0^r \rho_i(s) 4\pi s^2 ds. \quad (8)$$

Since dPGS is negatively charged, $N_+(r)$ explicitly represents for the number of counterions located in a distance r away from the dPGS COM. It follows that the total accumulated charge is

$$Z_{\text{acc}}(r) = N_+(r) - N_-(r) - N_C(r), \quad (9)$$

which gives the accumulated dPGS charge deduced from the structural one by adding the ionic shell.

For the definition of the effective charge of a dendrimer (and thus the effective surface potential) we take the basic Debye-Hückel (DH) theory for the radial electrostatic potential distribution around a charged sphere with radius r_{eff} and valency Z_{eff} as reference,⁴⁷

$$e\beta\phi_{\text{DH}}(r) = Z_{\text{eff}} l_B \frac{e^{\kappa r_{\text{eff}}}}{1 + \kappa r_{\text{eff}}} \frac{e^{-\kappa r}}{r}, \quad (10)$$

where e is the elementary charge and $\kappa = \sqrt{8\pi l_B c_0}$ is the inverse Debye length for a symmetric, monovalent salt. This solution is derived with the Dirichlet boundary condition, *i.e.*, fixing the surface potential $\phi(r_{\text{eff}})$ and the one far away $\phi(\infty) = 0$. The DH potential usually works well in the region far from the colloid, where nonlinear effects, such as ion–ion correlations and condensation, become irrelevant. For the “correlated Stern layer” at the interface of the charged sphere, the electrostatic potential ϕ is expected to deviate strongly from the DH potential ϕ_{DH} and all nonlinear effects are adsorbed into the effective charge Z_{eff} (as, e.g., based on solutions of the full non-linear Poisson-Boltzmann theory^{44–48}). By taking the logarithm of eq. (10) and mapping directly on the far-field behavior of the electrostatic decay calculated in the simulation, the double-layer behavior can be quantified with high accuracy.⁶⁷ This provides also the basis to define the position of the Stern layer, or better expressed, the exact location r_{eff} of the interface between the diffusive double layer in the DH sense and the correlated condensed ion layers. The effective surface potential is then simply $\phi_0 = \phi_{\text{DH}}(r_{\text{eff}})$.

Table 3: Properties of dPGS of generation G_n in the experiments. The dPGS weight $M_{n,\text{dPGS}}$ is deduced from the respective core weight $M_{n,\text{dPG}}$ and sulfate group number N_{ter} . DS is the degree of sulfation, and PDI is the polydispersity index. η is the ζ -potential attained from the electrophoretic experiment.

| Label | G ₂ | G ₄ | G _{4.5} | G _{5.5} |
|-----------------------------|----------------|----------------|------------------|------------------|
| $M_{n,\text{dPG}}$ [kD] | 2 | 7 | 10 | 20 |
| PDI | 1.7 | 1.7 | 1.5 | 1.2 |
| DS [%] | 100 | 100 | 99 | 98 |
| N_{ter} | 28 | 102 | 135 | 266 |
| $M_{n,\text{dPGS}}$ [kD] | 5 | 18 | 24 | 47 |
| η [mV] | -47.71 | -58.46 | -58.73 | -70.9 |

2.6. Experimental Materials and Methods. Dendritic polyglycerol (dPG) was synthesized by anionic ring opening polymerization of glycidol.⁶⁸ Gel permeation chromatography (GPC) is employed to measure the number averaged molecular weight of the core $M_{n,\text{dPG}}$ and Polydispersity index (PDI). Afterwards dPGS was prepared by the sulfation of dPG with SO₃-pyridine complex in dimethylformamide (DMF) according to reported procedure.⁶⁹ The degree of sulfation (DS) was

determined by elemental analysis. Properties of dPGS in different generations are summarized in Tab. 3.

Size and ζ -potential (electrophoretic mobility) measurements were performed with a Zetasizer Nano ZS instrument (ZEN 3500, Malvern Instruments, Herrenberg, Germany) equipped with a 18 mW He-Ne laser ($\lambda=633$ nm). The molecule size r_{hd} was measured by dynamic light scattering (DLS) in UV-transparent disposable cuvettes (VWR, Germany) at a back scattering angle of 173° . The compounds were dissolved in 10 mM MOPS buffer (adding NaCl to adjust ionic strength to 10 mM) pH 7.4 at concentration of 1 mg/ml and were filtered through $0.8 \mu\text{m}$ polyethersulfone syringe filter (PALL, USA). Prior to measurement, each sample was equilibrated for 2 min at 37° and measured with 10 scans each lasting for 10 s. The stated values for the hydrodynamic diameter are the mean of three independent measurements. The electrophoretic mobility was measured at 5 mg/ml in the same buffer as above also in three independent measurements (with all values reported in the SI). The solutions were filtered through $0.2 \mu\text{m}$ polyethersulfone syringe filter and equilibrated for 10 min at 37° in folded DTS 1060 capillary cells (Malvern, UK). The shown data for the ζ -potential in the resulting figure are based on the Henry function with the Ohshima approximation

$$f(\kappa r_{hd}) = 1 + \frac{1}{2[1 + \delta/(\kappa r_{hd})]^3}, \quad (11)$$

with $\delta = (5/2)[1 + 2 \exp(-\kappa r_{hd})]^{-1}$ for the conversion of mobilities to potentials.⁷⁰ The following reported ζ -potential are the mean of the three independent measurements.

3. RESULTS AND DISCUSSION

3.1. Size, sphericity and molecular density distributions.

3.1.1 Radius of gyration and asphericity

The radius of gyration R_g of the dPGS macromolecules as a function of generation n is summarized in Table 4. We find that R_g increases from 0.52 nm to 2.17 nm from G_0 to G_6 . A linear behavior is

Table 4: Snapshots and Parameters for the CG dPGS model. In the dPGS snapshots on the top, red and orange beads depict the terminal charged and inner neutral beads, respectively. N_{dPGS} and N_{ter} stand for the total number of CG segments and terminal sulfate (C) beads for dPGS, respectively. We assign $Z_{\text{bar}} = -N_{\text{ter}}$, r_d and R_g as dPGS bare charge, radius, and radius of gyration, respectively. Z_{eff} and r_{eff} define the dPGS effective charge and corresponding radius. Via the inflection point criterion,^{47,51} we can calculate the inflection dPGS radius r_{inf} and accordingly the inflection dPGS charge Z_{inf} . Finally, $\sigma_d = Z_{\text{bar}}/(4\pi r_d^2)$, $\sigma_{\text{eff}} = Z_{\text{eff}}/(4\pi r_{\text{eff}}^2)$ and $\sigma_{\text{inf}} = Z_{\text{inf}}/(4\pi r_{\text{inf}}^2)$ denote the bare, effective surface charge density, and inflection surface charge density, respectively. At the dPGS surface, we assign $\phi(r_{\text{eff}})$ as the surface potential. All the estimates are made given a salt concentration of $c_0 = 10$ mM.

| |  |  |  |  |  |  |  |
|--|---|---|---|---|---|---|---|
| Label | G ₀ | G ₁ | G ₂ | G ₃ | G ₄ | G ₅ | G ₆ |
| MW [KDa] | 0.79 | 1.72 | 4.10 | 8.32 | 16.77 | 33.67 | 68.00 |
| N_{dPGS} | 10 | 22 | 46 | 94 | 190 | 382 | 766 |
| N_{ter} | 6 | 12 | 24 | 48 | 96 | 192 | 384 |
| $Z_{\text{bar}} [e]$ | -6 | -12 | -24 | -48 | -96 | -192 | -384 |
| R_g [nm] | 0.52 | 0.71 | 0.92 | 1.16 | 1.43 | 1.76 | 2.17 |
| r_d [nm] | 0.65 | 0.83 | 1.10 | 1.35 | 1.65 | 2.05 | 2.55 |
| $\sigma_d [e/\text{nm}^{-2}]$ | -1.28 | -1.34 | -1.58 | -2.10 | -2.81 | -3.64 | -4.70 |
| r_{eff} [nm] | 0.7 | 1.6 | 1.9 | 2.4 | 2.8 | 3.3 | 3.8 |
| $Z_{\text{eff}} [e]$ | -6.0 | -7.3 | -10.6 | -14.3 | -18.7 | -24.5 | -32.9 |
| $\sigma_{\text{eff}} [e/\text{nm}^{-2}]$ | -0.97 | -0.23 | -0.23 | -0.20 | -0.19 | -0.18 | -0.18 |
| $\phi(r_{\text{eff}}) [k_B T]$ | -4.20 | -2.12 | -2.37 | -2.22 | -2.28 | -2.25 | -2.40 |
| r_{inf} [nm] | – | 1.1 | 1.5 | 1.8 | 2.1 | 2.6 | 3.1 |
| $Z_{\text{inf}} [e]$ | – | -9.9 | -14.9 | -22.9 | -37.5 | -52.2 | -85.8 |
| $\sigma_{\text{inf}} [e/\text{nm}^{-2}]$ | – | -0.65 | -0.53 | -0.56 | -0.68 | -0.62 | -0.71 |

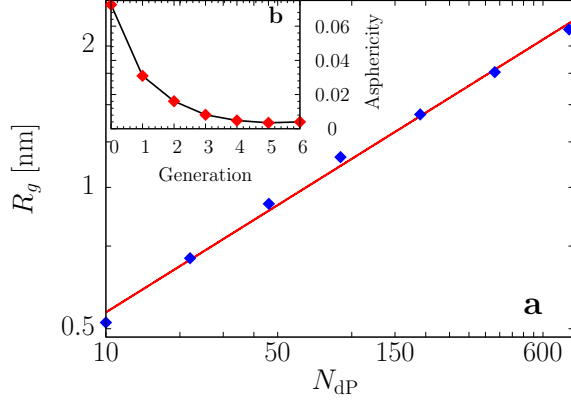


Figure 3: (a) Log–log plot of the radius of gyration R_g versus the total beads number N_{dP} for generations G_0 to G_6 . The red line is the fitted power law function $R_g \sim N_{\text{dP}}^{0.33}$ for all generations, while the dotted cyan line is a fitted power law function $R_g \sim N_{\text{dP}}^{0.30}$ for generations G_2 to G_6 only. Inset (b): the asphericity parameter A (bottom panel) versus generation of the CG dPGS molecules.

revealed in a log–log plot of R_g in terms of the total number of the CG segments, N_{dP} , in Fig 3(a). Hence, the dPGS size follows the scaling law $R_g \sim N_{\text{dP}}^\nu$, where we find the scaling exponent $\nu = 0.33$ if we fit all generations, while it decreases slightly to $\nu = 0.30$ if we only fit through the larger generations G_2 to G_6 , cf. Fig 3(a). Such a scaling close to $1/3$ is fully consistent with the now well established ‘dense-core’ picture of dendrimers, where details, however, can depend on the particular dendrimer architecture, see the deeper discussions in exemplary previous work.^{1,3,37,41}

In Fig 3(b), we plot the asphericity versus the generation number. For all inspected generations we find values lower than $A \sim 0.07$, which suggests an almost perfect spherical shape for dPGS molecules. Larger generations show higher sphericity, very likely due to a more homogeneous distribution of the larger number of closer packed beads and a thus higher compactness. We show snapshots of the CG dendrimers for all investigated generations G_0 to G_6 in Table 4.

3.1.2 Density distributions and ‘intrinsic’ radius

Figure 4 shows the radial density distributions $\rho_i(r)$ of selected components with respect to the distance r to the dendrimer core bead. Fig 4(a) shows the distribution of the terminal sulfate beads. For the smaller generations $G < 4$, we find a single-peaked distribution, corresponding to the picture that most of the charged terminal beads stay on the molecular surface.^{30,31,39,41} For the

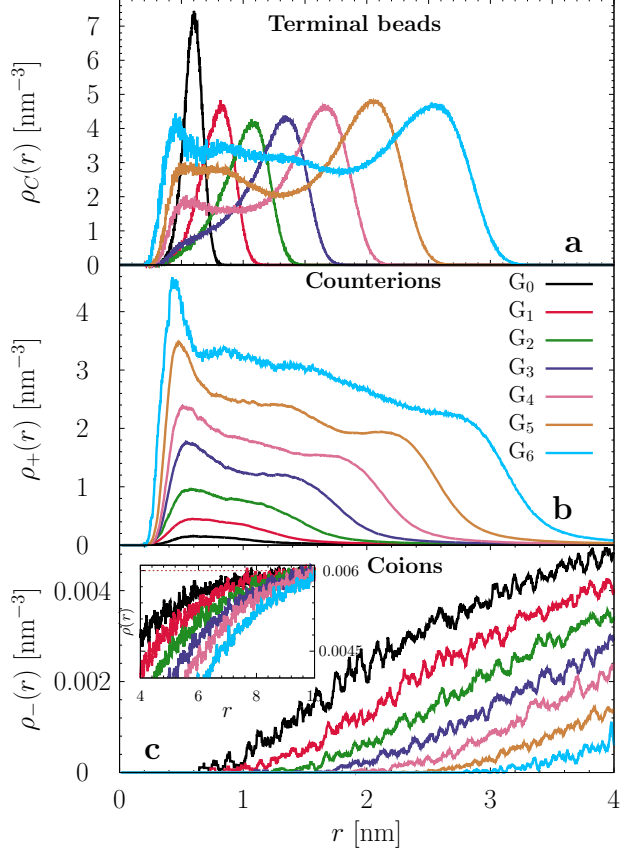


Figure 4: Radial density distribution $\rho_i(r)$ with respect to the dPGS core of (a) the terminal sulfate beads, $i = C$, (b) the cations (counterions; $i = +$), and (c) the anions (coions; $i = -$) for generations G_0 to G_6 . In the inset of panel (c) we show the anion density profile at longer distance up to $r = 10$ nm, with the limiting bulk anion density c_0 marked by a dashed horizontal line.

larger generations, however, a bimodal distribution signified by a small peak at $r \approx 0.6$ nm appears, indicating a small number of dendrons backfolding toward the dendrimer core. (Better visible in density plots re-scaled to refer to the position of the sulfate peak, see the SI.) The backfolding effect was already detected for other terminally-charged CG dendrimer models^{30,31,39,41} contributing to a dense-core in contrast to a dense-shell arrangement.¹ An ‘intrinsic’ dPGS radius r_d can be roughly deduced from the location of maximum density of the terminal groups. As implied in Fig. 4(a), we find a dPGS radius $r_d^{G_0} \approx 0.6$ nm for generation G_0 increasing to $r_d^{G_6} \approx 2.6$ nm for generation G_6 . All values are summarized in Table 4.

The radial density $\rho_+(r)$ of the cations, shown in Fig. 4(b), is found to have qualitatively the expected response to the distribution of terminal beads and follows roughly the sulfate distribution.

In particular, for all generations $\rho_+(r)$ decreases as expected in an exponential (Yukawa or DH-like) fashion to the bulk concentration for large distances. For closer distances, $r \simeq r_d$ highly nonlinear effects are visible, e.g., in the response to the backfolding of the terminal beads we observe the enrichment of cations at $r \simeq 0.5$ nm inside the dPGS, corresponding to the lower sulfate peaks close to the core in Fig. 4(a). On the contrary and as expected, coions are repelled by the dPGS due to the electrostatic repulsion.

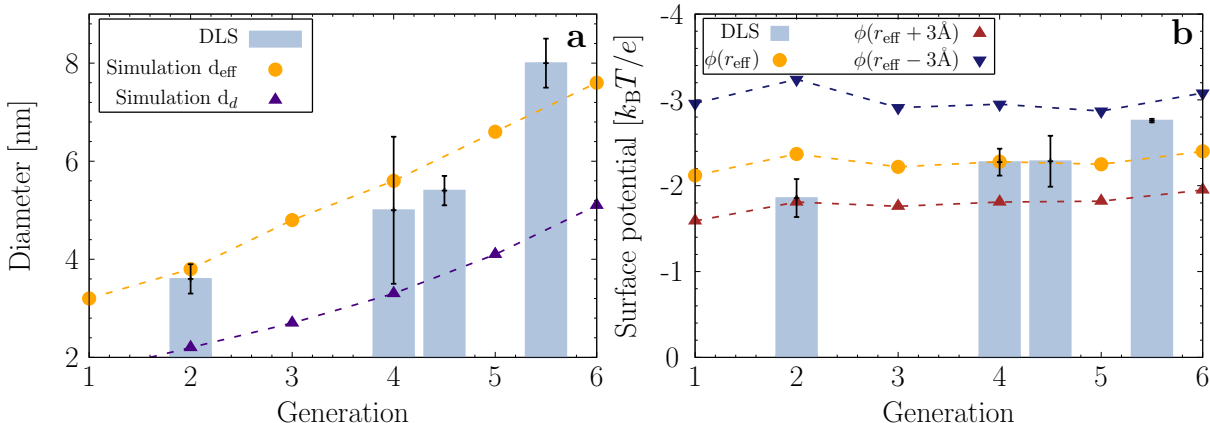


Figure 5: (a) Hydrodynamic diameter and (b) surface potential as determined via Zetasizer measurements (blue bars) and simulations (symbols; dashed lines are guided to the eye). In a) the simulation results are plotted for the intrinsic dPGS diameter $d_d = 2r_d$ and the effective diameter $d_{\text{eff}} = 2r_{\text{eff}}$. In b) simulation results are plotted for the effective surface potential $\phi_{\text{eff}} = \phi(r_{\text{eff}})$ at the location r_{eff} and that at one solvation layer shifted, i.e., $r_{\text{eff}} + 0.3$ nm and $r_{\text{eff}} - 0.3$ nm, respectively.

In Fig 5(a), we plot the hydrodynamic diameter measured via Zetasizer experiments of generation 2, 4, 4.5 and 5.5, respectively. As expected it increases with the molecular weight. A comparison to the dPGS size estimated from the sulfate peak in Fig. 4(a) from the simulation, $2r_d$, shows not a good agreement, probably because the correlated solvation layer, i.e., the Stern layer, is relatively thick and reaches out further into the bulk. The analysis in the next section, where an effective dPGS radius based on the ionic charge distribution is calculated, fully supports this conjecture.

3.2. Electrostatic properties of dPGS.

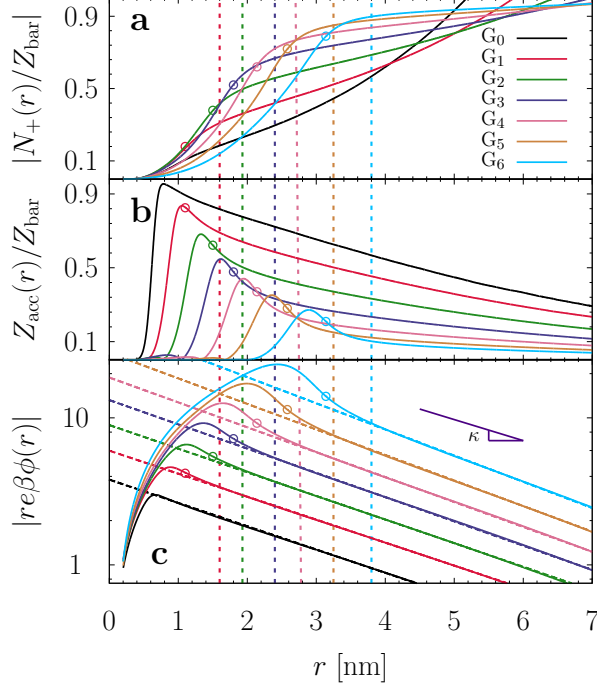


Figure 6: Distance-resolved (a) normalized running coordination number of counterions N_+/Z_{bar} , (b) normalized accumulated effective charge $Z_{\text{acc}}(r)/Z_{\text{bar}}$, (c) the product of distance r and dimensionless radial electrostatic potential $|re\beta\phi|$. We put a log-scale in (c) at the y-axis to examine the exponential decay. The long dashed line in (c) are fits according to the DH potential ϕ_{DH} , see Eq.(10). The vertical dashed lines signify the effective radius r_{eff} of dPGS, whereas the circles mark the inflection radius r_{inf} . The dPGS generation for that plot ranges from 0 to 6 in condition of salt concentration $c_0 = 10$ mM. The exponential decay with standard inverse DH length $\kappa = 0.33 \text{ nm}^{-1}$ derived by DH theory is plot in panel (c) as a further comparison.

3.2.1 Electrostatic potential, charge renormalization and effective ‘charge’ radius

From the ionic density profiles we can now in detail investigate local charge accumulation and electrostatic potential distributions. The accumulated number $N_+(r)$ of counterions and the locally total accumulated dPGS charge $Z_{\text{acc}}(r)$ (i.e., the local effective charge according to Eq. (9)) are presented in Fig 6(a) and Fig 6(b), respectively. It is found that both $N_+(r)$ and $Z_{\text{acc}}(r)$ increase sharply with distance r from the dPGS core due to the rising accumulation of charged beads. While $N_+(r)$ naturally rises, $Z_{\text{acc}}(r)$ jumps to a maximum at a distance r_Z and drops gradually. At this distance, a large portion of the sulfate charges are neutralized by counterions. As implied by Fig 6(b), we find for instance that more than 70% of the charges at $r = r_Z$ for G_6 are compensated by bound counterions. This charge renormalization effect has been extensively studied at hand of

simple charged spheres with smooth surfaces, and theories for the effective charge and size have been developed.^{44,47,48,50,51} One important outcome is that one can define the critical location for counterion-condensation in terms of the inflection point in a plot of Z_{acc} as a function of the inverse radial distance $1/r$.^{47,51} The equation $d^2 Z_{\text{acc}}/d(1/r)^2|_{r=r_{\text{inf}}} = 0$ leads to the inflection radius, r_{inf} , within ions are deemed condensed. We marked r_{inf} by circle symbols for all generations in Fig 6. Note that r_{inf} is larger than r_Z and could be used to read off an effective charge size and charge of the macromolecule.

A more practical concept to define an effective size and charge is to quantitatively map the double-layer decay of the potential onto the basic DH-theory, Eq. (10). Fig. 6(c) plots the rescaled potential $|re\beta\phi|$ versus distance r in a log-linear scale. For the potential far away a homogeneously charged sphere, the DH potential ϕ_{DH} with a renormalized charge should apply, yielding an exponential decay $e^{-\kappa(n)r}/r$ attributed to the electrostatic screening. The plot indeed shows the expected linear decay at large separations unambiguously for all presented dPGS with a slope as expected to be close to the standard inverse DH length $\kappa = 0.33 \text{ nm}^{-1}$ for the salt concentration $c_0 = 10 \text{ mM}$. In detail, we find slopes of $\kappa(n)$ to monotonically increase with n from $\kappa(0) = 0.36 \text{ nm}^{-1}$ to $\kappa(6) = 0.41 \text{ nm}^{-1}$. That slight increase is due to the increasing number of counterions in the finite system which also contribute to screening. In contrast to the simple exponential decay at large separations, for smaller distances the potential term $|re\beta\phi(r)|$ climbs up quickly with decreasing distance r to a maximum before it decays to almost vanishing potential close to the dPGS core. This highly nonlinear behavior is expected from the high electrostatic and steric correlations between sulfate beads and counterions in this dense Stern layer.

As indicated by Fig. 6(c), the potential can now be naturally divided into two parts: a DH-regime $r > r_{\text{eff}}$, where the DH potential describes correctly the potential, and a non-DH regime $r_d < r < r_{\text{eff}}$, where a non-monotonic and highly non-exponential behavior is revealed. In that sense, r_{eff} now acts as a measure of the dPGS effective radius at which we can attain an effective dPGS charge Z_{eff} ⁴⁷ (see also the SI). We depict the position of the DH radius r_{eff} by vertical dashed lines in Fig 6. We list r_{eff} and Z_{eff} in the Table 4 for generations 0 to 6. We find an increase of

both r_{eff} and Z_{eff} with dPGS generation index and substantial charge renormalization effects. For instance, the bare charge for G_6 -dPGS is $-384 e$ (still presents at a radius r_d , cf. Fig. 5(b)) is effectively renormalized to $Z_{\text{eff}} = -32.9 e$ at large distances $r > r_{\text{eff}}$. An exception is G_0 in which case we find $r_d \approx r_{\text{eff}}$ and hardly any renormalization by condensed counterions takes places. In agreement, the accumulated counterions profile N_+ for G_0 in Fig 6(a) reveals DH behavior almost in the full range of r and no inflection radius could be identified.

Note that both r_{inf} and r_{eff} can in principle be taken as definition for the effective size and charge of the charge-renormalized sphere. Although the difference between them appears not so large in Fig. 6, still a significant charge renormalization happens in between as the gradient $dN_+(r)/dr$ at r_{inf} is relatively large, *i.e.*, there is a marked density decrease of the counterions from distance r_{inf} to r_{eff} . In the following, we base our analysis only on r_{eff} as we believe that the inflection point criterion holds only for more idealized systems (smooth surfaces, no salt). The procedure to obtain r_{eff} rests on the assumption that we can treat the dPGS as simple DH spheres, so it exactly serves our purpose. Interestingly, a comparison of the corresponding effective diameter, $2r_{\text{eff}}$ to the size measured in the Zetasizer experiments in Fig 5(a) shows satisfying agreement. This demonstrates that the thickness of the correlated Stern layer in our simulation is of reasonable size and resembles the size of the bound solvation layer revealed by the experiments.

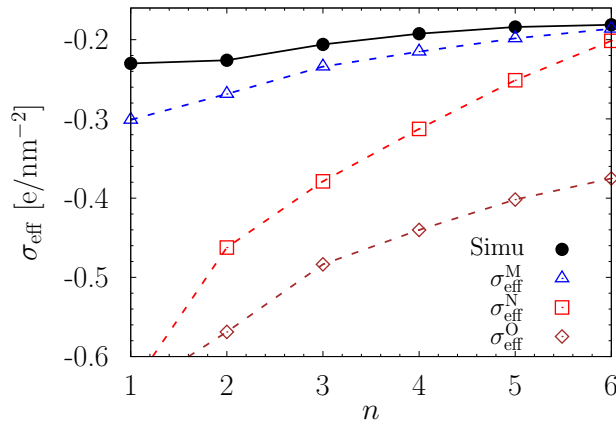


Figure 7: dPGS effective surface charge density $\sigma_{\text{eff}} = Z_{\text{eff}}/(4\pi r_{\text{eff}}^2)$ versus dPGS generation number n . The solid circles are simulation results ranging from G_1 to G_6 . The empty upward triangles, squares, diamonds are effective charge based on various theories as expressed by σ_{M} , σ_{N} , σ_{O} in eqs. (13), Eq. (14), and Eq. (12), respectively.

3.2.2 Effective surface charge density and potential

Considering the intrinsic radius r_d and the DH radius r_{eff} , the estimates of Z_{bar} and Z_{eff} lead to the dPGS bare surface charge density σ_d and effective surface charge density $\sigma_{\text{eff}} = Z_{\text{eff}}/(4\pi r_{\text{eff}}^2)$, respectively. Numbers are also summarized in Table 4. We find a monotonic decrease on σ_d with generation n , in response to the growing number of the surface beads. (The small portion of backfolding terminal beads increasing with generation decreases the surface charge valency slightly but not significant). Due to the large counterion-binding and charge renormalization effect, the effective charge density σ_{eff} is about one order of magnitude smaller than the bare one. Interestingly, it virtually remains constant, even slightly decreases from $-0.23 e \text{ nm}^{-2}$ for G_1 to a saturated value $-0.18 e \text{ nm}^{-2}$ for G_5 and G_6 . Experiments of carboxyl-terminated dendrimers at pH much larger than the pKa (i.e., almost full ionization) also found higher effective charge densities of a lower generation G_2 than for G_5 .⁵²

The results for the effective surface charge can be compared to available theories of charge renormalization of highly charged spheres, typically valid in low or high salt limits. Early approaches are based on approximate solutions of the nonlinear Poisson-Boltzmann equation for isolated spheres at infinite dilution, e.g., improvements of the now classical Ohshima potential⁴⁴ lead to⁴⁸

$$\sigma_{\text{eff}}^{\text{O}} = \frac{-2e[1 + \kappa(n)r_{\text{eff}}]^2}{\pi l_B r_{\text{eff}} [1 + 2\kappa(n)r_{\text{eff}}]} \quad (12)$$

and should be valid for large $\kappa r_{\text{eff}} \gtrsim 1$, i.e., large spheres and/or high screening by salt. In the framework of standard counterion-condensation theory, Manning later derived a different but related expression for the saturation surface charge density of an isolated sphere in the same regime ($\kappa r_{\text{eff}} \rightarrow 0$) as⁵⁰

$$\sigma_{\text{eff}}^{\text{M}} = \frac{e[1 + \kappa(n)r_{\text{eff}}] \ln[\kappa(n)l_B]}{2\pi l_B r_{\text{eff}}}. \quad (13)$$

In the other limit ($\kappa r_{\text{eff}} \rightarrow 0$), Netz *et al.*⁴⁹ instead provide an estimate on the effective charge density explicitly dependent on the bare charge valency, Z_{bar} , by means of variational techniques,

via

$$\sigma_{\text{eff}}^{\text{N}} = \frac{-e}{4\pi r_d l_{\text{B}}} \ln \left(\frac{l_{\text{B}} |Z_{\text{bar}}|}{r_d^3 \kappa^2} \right). \quad (14)$$

For our dPGS systems, intermediate values $0.25 < \kappa r_{\text{eff}} < 1.6$ are established, for which an accurate analytical description apparently is difficult to achieve. We plot σ_{eff} in terms of generation number n , together with $\sigma_{\text{eff}}^{\text{M}}$, $\sigma_{\text{eff}}^{\text{N}}$ and $\sigma_{\text{eff}}^{\text{O}}$ in Fig. 7. We find that simulation and theory both yield the same trend, i.e., the absolute effective surface charge density decreases with generation n . Given the enormous charge renormalization effects of about one order of magnitude, the agreement to all theories is actually satisfactory, especially for the Manning theory. The relative error with respect to the magnitude of the bare surface charge is thus less than 10%. Based on this empirical comparison, the Manning approach can thus serve as a simple and analytical extrapolation to other systems and experiments.

Correspondingly, we define the dPGS surface potential $\phi(r_{\text{eff}})$, also summarized in Table 4. Similarly as the effective surface charge the surface potential is staying relatively constant with generation number. An inspection and comparison to ζ -potentials derived from our electrophoretic mobility experiments is made in Fig 5(b). Recall that the shear plane, where the ζ -potential is located, should lie beyond the Stern layer which refers to a position very close to r_{eff} where our effective surface potential $\phi(r_{\text{eff}})$ is in the simulation.^{71,72} Indeed, as we see in Fig 5(b), $\phi(r_{\text{eff}})$ reproduces the experimental ζ -potential very well at all generations. The sources of the remaining deviations can be of various origin, e.g., missing explicit water contributions to the electrostatic potential in the CG simulations or simply the lack of the exact knowledge of the shear plane. If, for instance, we assume an up- or down-shift of the location of the shear plane only about one solvation layer, say to be $\simeq r_{\text{eff}} \pm 0.3$ nm, the experimental range is well matched, cf. Fig 5(b). Note also that in the experiments not directly the potential is measured but the electrophoretic mobility (presented in the SI) and their conversion is based on idealized models.^{52,73}

We finally inspect the dependence of the effective dPGS radius r_{eff} and charge density σ_{eff} on the salt concentration. We plot the radial electrostatic potential $|re\beta\phi|$ for G₅-dPGS under three salt concentrations $c = 10$ mM, 100 mM, and 200 mM in Fig. 8. As one can see the exponential regime

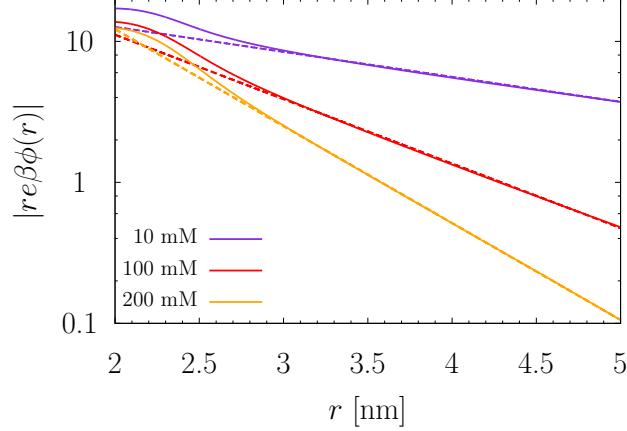


Figure 8: Log-linear plot of the distance-resolved G_5 -dPGS radial electrostatic potential times distance, $|re\beta\phi|$, as in Fig. 6(c), but now for different salt concentrations $c = 10, 100,$ and 200 mM. The dashed lines depict the corresponding DH potential ϕ_{DH} after fitting to the linear decay regime.

$\exp(-\kappa r)$ for large distances survives for all cases. Interestingly, a similar $r_{\text{eff}} \simeq 3.2$ nm is found with hardly any dependence on the salt concentration. The effective surface charge density goes down from $\sigma_{\text{eff}} = -0.18 e/\text{nm}^{-2}$ (10 mM) to $\sigma_{\text{eff}} = -0.14 e/\text{nm}^{-2}$ (100 mM) and $\sigma_{\text{eff}} = -0.10 e/\text{nm}^{-2}$ at 200 mM. Eq. (12) predicts an opposite trend than that and than Eqs. (13) and (14). The latter two treatments consistently point to the generic screening effect leading to a smaller surface potential $\phi(r_{\text{eff}})$ for higher salt concentrations.

4. CONCLUSIONS

In summary, we have investigated the electrostatic (surface) properties of highly charged dendrimers for various generations at hand of the biomedically important dPGS polyelectrolyte. We have defined an effective charge, effective surface charge and potential of dPGS for various generations and salt concentrations by a direct mapping procedure of the calculated electrostatic potentials onto the long-range Debye-Hückel-like electrostatic decay which defines the effective charge in its most practical level. The dPGS effective radius r_{eff} is accordingly addressed as a distance separating double-layer and condensation regimes and therefore gives the dPGS effective charge without ambiguity. Evidently, with that procedure the effective charge and the surface potential and their trends with generation can be consistently described by counterion-condensation theory

and show very good agreement with new experimental ζ -potential measurements as well.

In future, our model can be easily applied to dPGS-involved intermolecular interaction studies in biological context (e.g., binding to proteins or membranes), quantifying electrostatic interactions, in particular counterion-release effects on binding.⁷⁴⁻⁷⁶ Those studies could serve as important references to guide experiments and optimize dPG-based particles as a potent anti-inflammatory drug in biomedical applications. In particular, the strength of specific counterion binding and condensation has significant influence on binding affinity of dPGS or other charge-functionalized polyglycerol-based dendrimers, such a carboxylated or phosphorylated dPG.^{77,78}

Acknowledgement

Xiao Xu thanks the Chinese Scholar Council for financial support. The authors acknowledge fruitful discussions with Rohit Nikam and Rafael Roa Chamorro.

References

- (1) Ballauff, M.; Likos, C. N. Dendrimers in Solution: Insight from Theory and Simulation. *Angew. Chem., Int. Ed.* **2004**, *43*, 2998.
- (2) Lee, C. C.; MacKay, J. A.; Fréchet, J. M.; Szoka, F. C. Designing dendrimers for biological applications. *Nature Biotechnology* **2005**, *23*, 1517–1526.
- (3) Tian, W.; Ma, Y. Theoretical and computational studies of dendrimers as delivery vectors. *Chem. Soc. Rev.* **2013**, *42*, 705.
- (4) Khandare, J.; Calderón, M.; Dagiaa, N. M.; Haag, R. Multifunctional dendritic polymers in nanomedicine: opportunities and challenges. *Chem. Soc. Rev.* **2012**, *41*, 2824.
- (5) Maysinger, D.; Gröger, D.; Lake, A.; Licha, K.; Weinhart, M.; Chang, P. K.-Y.; Mulvey, R.; Haag, R.; McKinney, R. A. Dendritic Polyglycerol Sulfate Inhibits Microglial Activation and

- Reduces Hippocampal CA1 Dendritic Spine Morphology Deficits. *Biomacromolecules* **2015**, *16*, 3073–3082.
- (6) Reimann, S.; Gröger, D.; Kühne, C.; Riese, S. B.; Dervedde, J.; Haag, R. Shell Cleavable Dendritic Polyglycerol Sulfates Show High Anti-Inflammatory Properties by Inhibiting L-Selectin Binding and Complement Activation. *Adv. Healthcare Mater* **2015**, *4*, 2154–2162.
- (7) Gröger, D.; Paulus, F.; Licha, K.; Welker, P.; Weinhart, M.; Holzhausen, C.; Mundhenk, L.; Gruber, A. D.; Abram, U.; Haag, R. Synthesis and Biological Evaluation of Radio and Dye Labeled Amino Functionalized Dendritic Polyglycerol Sulfates as Multivalent Anti-Inflammatory Compounds. *Bioconjug. Chem.* **2013**, *24*, 1507–1514.
- (8) Vonnemann, J.; Beziere, N.; Böttcher, C.; Riese, S. B.; Kuehne, C.; Dervedde, J.; Licha, K.; von Schacky, C.; Kosanke, Y.; Kimm, M.; Meier, R.; Ntziachristos, V.; Haag, R. Polyglycerolsulfate Functionalized Gold Nanorods as Optoacoustic Signal Nanoamplifiers for In Vivo Bioimaging of Rheumatoid Arthritis. *Theranostics* **2014**, *4*, 629–641.
- (9) Sousa-Herves, A.; Würfel, P.; Wegner, N.; Khandare, J.; Licha, K.; Haag, R.; Welker, P.; Calderón, M. Dendritic polyglycerol sulfate as a novel platform for paclitaxel delivery: pitfalls of ester linkage. *Nanoscale* **2015**, *7*, 3923–3932.
- (10) Dervedde, J.; Rausch, A.; Weinhart, M.; Enders, S.; Tauber, R.; Licha, K.; Schirner, M.; Zügel, U.; von Bonin, A.; Haag, R. Dendritic polyglycerol sulfates as multivalent inhibitors of inflammation. *Proc. Natl. Acad. Sci. U. S. A.* **2010**, *107*, 19679–19684.
- (11) Hoshino, Y.; Lee, H.; Miura, Y. Interaction between synthetic particles and biomacromolecules: fundamental study of nonspecific interaction and design of nanoparticles that recognize target molecules. *Polym. J.* **2014**, *46*, 537.
- (12) Maiti, P. K.; Cagin, T.; Wang, G.; Goddard, W. A. Structure of PAMAM Dendrimers: Generations 1 through 11. *Macromolecules* **2004**, *37*, 6236.
- (13) Naylor, A. M.; Goddard, W. A.; Kiefer, G. E.; Tomalia, D. A. Starburst dendrimers. 5. Molecular shape control. *J. Am. Chem. Soc.* **1989**, *111*, 2339–2341.
- (14) Lee, I.; Athey, B. D.; Wetzel, A. W.; Meixner, W.; James R. Baker, J. Structural molecular

- dynamics studies on polyamidoamine dendrimers for a therapeutic application: effects of pH and generation. *Macromolecules* **2002**, *35*, 4510–4520.
- (15) Han, M.; Chen, P.; Yang, X. Molecular dynamics simulation of PAMAM dendrimer in aqueous solution. *Polymer* **2005**, *10*, 3481.
- (16) Maiti, P. K.; Cagin, T. T.; Lin, S.-T.; Goddard, W. A. Effect of Solvent and pH on the Structure of PAMAM Dendrimers. *Macromolecules* **2005**, *38*, 979–991.
- (17) Maiti, P. K.; Messina, R. Counterion Distribution and ζ -Potential in PAMAM Dendrimer. *Macromolecules* **2008**, *41*, 5002.
- (18) Murat, M.; Grest, G. S. Molecular Dynamics Study of Dendrimer Molecules in Solvents of Varying Quality. *Macromolecules* **1996**, *29*, 1278.
- (19) Welch, P.; Muthukumar, M. Tuning the Density Profile of Dendritic Polyelectrolytes. *Macromolecules* **1998**, *31*, 5892.
- (20) Lyulin, S. V.; Evers, L. J.; van der Schoot, P.; Darinskii, A. A.; Lyulin, A. V.; Michels, M. A. J. Effect of Solvent Quality and Electrostatic Interactions on Size and Structure of Dendrimers. Brownian Dynamics Simulation and Mean-Field Theory. *Macromolecules* **2004**, *37*, 3049–3063.
- (21) Lyulin, S. V.; Darinskii, A. A.; Lyulin, A. V.; Michels, M. A. J. Computer Simulation of the Dynamics of Neutral and Charged Dendrimers. *Macromolecules* **2004**, *37*, 4676–4685.
- (22) Giupponi, G.; Buzza, D. M. A. Monte Carlo simulation of dendrimers in variable solvent quality. *J. Chem. Phys.* **2004**, *120*, 10290.
- (23) Lee, H.; Larson, R. G. Molecular Dynamics Simulations of PAMAM Dendrimer-Induced Pore Formation in DPPC Bilayers with a Coarse-Grained Model. *J. Phys. Chem. B* **2006**, *110*, 18204–18211.
- (24) Lee, H.; Larson, R. G. Coarse-grained molecular dynamics studies of the concentration and size dependence of fifth- and seventh-generation PAMAM dendrimers on pore formation in DMPC bilayer. *J. Phys. Chem. B* **2008**, *112*, 7778–7784.
- (25) Lee, H.; Larson, R. G. A molecular dynamics study of the structure and inter-particle inter-

- actions of polyethylene glycol-conjugated PAMAM dendrimers. *J. Phys. Chem. B* **2009**, *113*, 13202–13207.
- (26) Chong, L.; Aydin, F.; Dutt, M. Implicit solvent coarse-grained model of polyamidoamine dendrimers: Role of generation and pH. *J. Comput. Chem.* **2016**, *37*, 920–926.
- (27) Gurtovenko, A. A.; Lyulin, S. V.; Karttunen, M.; Ilpo Vattulainen, Molecular dynamics study of charged dendrimers in salt-free solution: Effect of counterions. *J. Chem. Phys.* **2006**, *124*, 094904.
- (28) Blaak, R.; Lehmann, S.; Likos, C. N. Charge-Induced Conformational Changes of Dendrimers. *Macromolecules* **2008**, *41*, 4452–4458.
- (29) Carbone, P.; Lue, L. Prediction of Bulk Density and Molecular Packing in Model Dendrimers with Different Chain Stiffness. *Macromolecules* **2010**, *43*, 9191–9197.
- (30) Huißmann, S.; Wynveen, A.; Likos, C. N.; Blaak, R. The effects of pH, salt and bond stiffness on charged dendrimers. *J. Phys.: Condens. Matter* **2010**, *22*, 232101.
- (31) Huißmann, S.; Wynveen, A.; Likos, C. N.; Blaak, R. Conformations of high-generation dendritic polyelectrolytes. *J. Mat. Chem.* **2010**, *20*, 10486–10494.
- (32) Tian, W.; Ma, Y. pH-responsive dendrimers interacting with lipid membranes. *Soft Matter* **2012**, *8*, 2627.
- (33) Das, A. K.; Hsiao, P.-Y. Charged Dendrimers in Trivalent Salt Solutions under the Action of DC Electric Fields. *J. Phys. Chem. B* **2014**, *118*, 6265–6276.
- (34) Welch, P.; Muthukumar, M. Dendrimer-Polyelectrolyte Complexation: A Model Guest-Host System. *Macromolecules* **2000**, *33*, 6159.
- (35) Lenz, D. A.; Blaak, R.; Likos, C. N. Structural properties of dendrimer-colloid mixtures. *J. Phys.: Condens. Matter* **2012**, *24*, 284119.
- (36) Kłos, J. S.; Sommer, J.-U. Properties of Dendrimers with Flexible Spacer-Chains: A Monte Carlo Study. *Macromolecules* **2009**, *42*, 4878.
- (37) Maiti, P. K.; Li, Y.; Cagin, T.; Goddard, W. A. Structure of polyamidoamide dendrimers up to limiting generations: A mesoscale description. *J. Chem. Phys.* **2009**, *130*, 144902.

- (38) Tian, W.; Ma, Y. Coarse-grained molecular simulation of interacting dendrimers. *Soft Matter* **2011**, *7*, 500.
- (39) Kłos, J. S.; Sommer, J.-U. Simulations of Terminally Charged Dendrimers with Flexible Spacer Chains and Explicit Counterions. *Macromolecules* **2010**, *43*, 4418–4427.
- (40) Kłos, J. S.; Sommer, J.-U. Monte Carlo simulations of charged dendrimer-linear polyelectrolyte complexes and explicit counterions. *J. Chem. Phys.* **2011**, *134*, 204902.
- (41) Kłos, J. S.; Sommer, J.-U. Simulations of Neutral and Charged Dendrimers in Solvents of Varying Quality. *Macromolecules* **2013**, *46*, 3107–3117.
- (42) Huißmann, S.; Likos, C. N.; Blaak, R. Explicit vs Implicit Water Simulations of Charged Dendrimers. *Macromolecules* **2012**, *45*, 2562.
- (43) Tian, W.; Ma, Y. Effects of valences of salt ions at various concentrations on charged dendrimers. *Soft Matter* **2010**, *6*, 1308.
- (44) Ohshima, H.; Healy, T. W.; White, L. R. Accurate analytic expressions for the surface charge density/surface potential relationship and double-layer potential distribution for a spherical colloidal particle. *J. Colloid Interface Sci.* **1982**, *90*, 17–26.
- (45) Alexander, S.; Chaikin, P. M.; Grant, P.; Morales, G. J.; Pincus, P. Charge renormalization, osmotic pressure, and bulk modulus of colloidal crystals: Theory. *J. Chem. Phys.* **1983**, *80*, 5776.
- (46) Ramanathan, G. V. Counterion condensation in micellar and colloidal solutions. *J. Chem. Phys.* **1988**, *88*, 3887.
- (47) Belloni, L. Ionic condensation and charge renormalization in colloidal suspensions. *Colloids Surf., A* **1998**, *140*, 227–243.
- (48) Bocquet, L.; Trizac, E.; Aubouy, M. Effective charge saturation in colloidal suspensions. *J. Chem. Phys.* **2002**, *117*, 8138.
- (49) Netz, R.; Orland, H. Variational charge renormalization in charged systems. *Eur. Phys. J. E* **2003**, *11*, 301.
- (50) Manning, G. S. Counterion Condensation on Charged Spheres, Cylinders, and Planes. *J. Phys.*

- Chem. B* **2007**, *111*, 8554–8559.
- (51) Gillespie, D. A. J.; Hallett, J. E.; Elujoba, O.; Hamzah, A. F. C.; Richardson, R. M.; Bartlett, P. Counterion condensation on spheres in the salt-free limit. *Soft Matter* **2014**, *10*, 566–577.
- (52) Huang, Q. R.; Dubin, P. L.; Moorefield, C. N.; Newkome, G. R. Counterion Binding on Charged Spheres: Effect of pH and Ionic Strength on the Mobility of Carboxyl-Terminated Dendrimers. *J. Phys. Chem. B* **2000**, *104*, 898–904
- .
- (53) Hess, B.; Kutzner, C.; van der Spoel, D.; Lindahl, E. GROMACS 4: Algorithms for Highly Efficient, Load-Balanced, and Scalable Molecular Simulation. *J. Chem. Theory Comput.* **2008**, *4*, 435–447.
- (54) Schuler, L. D.; Daura, X.; van Gunsteren, W. F. An improved GROMOS96 force field for aliphatic hydrocarbons in the condensed phase. *J. Comput. Chem.* **2001**, *22*, 1205–128.
- (55) Berendsen, H. J. C.; Grigera, J. R.; Straatsma, T. P. The missing term in effective pair potentials. *J. Phys. Chem.* **1987**, *91*, 6269–6271.
- (56) Frisch, M. J. e. a. Gaussian 09 Revision D.01. 2009; Gaussian Inc. Wallingford CT 2009.
- (57) Horta, B. A. C.; Fuchs, P. F. J.; van Gunsteren, W. F.; Hünenberger, P. H. New Interaction Parameters for Oxygen Compounds in the GROMOS Force Field: Improved Pure-Liquid and Solvation Properties for Alcohols, Ethers, Aldehydes, Ketones, Carboxylic Acids, and Esters. *J. Chem. Theory Comput.* **2011**, *7*, 1016–1031.
- (58) Jozica, D. GROMOS Developer. *Private Communication* **2013**,
- (59) Tang, X.; Koenig, P. H.; Larson, R. G. Molecular Dynamics Simulations of Sodium Dodecyl Sulfate Micelles in Water - The Effect of the Force Field. *J. Phys. Chem. B* **2014**, *118*, 3864–3880.
- (60) Evans, D. A. History of the Harvard ChemDraw Project. *Angew. Chem., Int. Ed.* **2014**, *53*, 11140.
- (61) Essmann, U.; Perera, L.; Berkowitz, M. L.; Darden, T.; Lee, H.; Pedersen, L. G. A smooth particle mesh Ewald method. *J. Chem. Phys.* **1995**, *103*, 8577.

- (62) Müller-Plathe, F. Coarse-graining in polymer simulation: from the atomistic to the mesoscopic scale and back. *ChemPhysChem* **2002**, *3*, 754.
- (63) Reith, D.; Pütz, M.; Müller-Plathe, F. Deriving effective mesoscale potentials from atomistic simulations. *J. Comput. Chem.* **2003**, *24*, 1624.
- (64) Smith, D. E.; Dang, L. X. Computer simulations of NaCl association in polarizable water. *J. Chem. Phys.* **1993**, *100*, 3757.
- (65) Kalcher, I.; Schulz, J. C. F.; Dzubiella, J. Electrolytes in a nanometer slab-confinement: Ion-specific structure and solvation forces. *J. Chem. Phys.* **2010**, *133*, 164511.
- (66) Voit, B. I. Dendritic polymers: from aesthetic macromolecules to commercially interesting materials. *Acta Polym.* **1995**, *46*, 87–99.
- (67) Kalcher, I.; Dzubiella, J. Structure - thermodynamics relation of electrolyte solutions. *J. Chem. Phys.* **2009**, *130*, 134507.
- (68) Sunder, A.; Hanselmann, R.; Frey, H.; Mülhaupt, R. Controlled synthesis of hyperbranched polyglycerols by ring-opening multibranching polymerization. *Macromolecules* **1999**, *32*, 4240–4246.
- (69) Türk, H.; Haag, R.; Alban, S. Dendritic polyglycerol sulfates as new heparin analogues and potent inhibitors of the complement system. *Bioconjugate chemistry* **2004**, *15*, 162–167.
- (70) Ohshima, H. Electrophoretic mobility of soft particles. *J Colloid Interface Sci* **1994**, *163*, 474–483.
- (71) Lyklema, J. *Fundamentals of interface and colloid science: vol. II, Solid-liquid interfaces*; Academic Press, London, 1995.
- (72) Ahualli, S.; Delgado, Á. V.; Carrique, F.; Jiménez, M. L. *AC Electrokinetics of Concentrated Suspensions of Soft and Hairy Nanoparticles: Model and Experiments*; John Wiley & Sons, Inc., 2016.
- (73) Hunter, R. J. *Foundations of Colloid Science*; Oxford University Press, Oxford, 2001.
- (74) Yu, S.; Xu, X.; , C.; van der Giet, M.; Zidek, W.; Jankowski, J.; Dzubiella, J.; Ballauff, M. Interaction of human serum albumin with short polyelectrolytes: a study by calorimetry and

- computer simulations. *Soft Matter* **2015**, *11*, 4630–4639.
- (75) Yigit, C.; Heyda, J.; Ballauff, M.; Dzubiella, J. Like-charged protein-polyelectrolyte complexation driven by charge patches. *J. Chem. Phys.* **2015**, *143*, 064905.
- (76) Yigit, C.; Kanduc, M.; Ballauff, M.; Dzubiella, J. Interaction of charged patchy protein models with like-charged polyelectrolyte brushes. *Langmuir* **2016**, *33*, 417–427.
- (77) Weinhart, M.; Gröger, D.; Enders, S.; Dervede, J.; Haag, R. Synthesis of Dendritic Polyglycerol Anions and Their Efficiency Toward L-Selectin Inhibition. *Biomacromolecules* **2011**, *12*, 2502–2511.
- (78) Weinhart, M.; Gröger, D.; Enders, S.; Riese, S. B.; Dervede, J.; Kainthan, R. K.; Brooks, D. E.; Haag, R. The Role of Dimension in Multivalent Binding Events: Structure-Activity Relationship of Dendritic Polyglycerol Sulfate Binding to L-Selectin in Correlation with Size and Surface Charge Density. *Macromol. Biosci.* **2011**, *11*, 1088–1098.

Graphical TOC Entry

